Magnetic dipole emission of Dy^{3+}:Y_2O_3 and Tm^{3+}:Y_2O_3 at near-infrared wavelengths

Christopher M. Dodson, Jonathan A. Kurvits, Dongfang Li, Mingming Jiang, and Rashid Zia*

School of Engineering and Department of Physics, Brown University, Providence, RI 02912
USA
**rashid_zia@brown.edu*

Abstract: Naturally occurring magnetic dipole resonances can be used as optical sources in metamaterials and optical nanostructures to engineer light emission with applications in energy harvesting, biological imaging, and other photonic devices. Here, we use energy-momentum spectroscopy to quantify the electric and magnetic dipole emission rates of near-infrared transitions in Dy^{3+} and Tm^{3+} doped Y_2O_3. Of these emission lines, we find that the overlapping $^4F_{9/2} \rightarrow {}^6F_{11/2}$ and $^4F_{9/2} \rightarrow {}^6H_{9/2}$ transitions in Dy^{3+} and the overlapping $^1G_4 \rightarrow {}^3H_5$ and $^3H_4 \rightarrow {}^3H_6$ transitions in Tm^{3+} exhibit the greatest MD emission and thus offer the most direct pathway for integration with magnetic modes in resonant nanostructures.

© 2014 Optical Society of America

OCIS codes: (300.2140) Spectroscopy, emission; (310.3840) Thin films, materials and process characterization.

References and links

1. C. M. Dodson and R. Zia, "Magnetic dipole and electric quadrupole transitions in the trivalent lanthanide series: Calculated emission rates and oscillator strengths," Phys. Rev. B **86**, 125102 (2012).
2. S. Derom, A. Berthelot, A. Pillonnet, O. Benamara, A. M. Jurdyc, C. Girard, and G. C. des Francs, "Metal enhanced fluorescence in rare earth doped plasmonic core–shell nanoparticles," Nanotechnology **24**, 495704 (2013).
3. S. E. Yoca and P. Quinet, "Decay rates for radiative transitions in the Pr IV spectrum," J. Phys. B–At. Mol. Opt. **46**, 145003 (2013).
4. S. E. Yoca and P. Quinet, "Relativistic Hartree–Fock calculations of transition rates for allowed and forbidden lines in Nd IV," J. Phys. B–At. Mol. Opt. **47**, 35002–35016 (2014).
5. N. Noginova, Y. Barnakov, H. Li, and M. A. Noginov, "Effect of metallic surface on electric dipole and magnetic dipole emission transitions in Eu^{3+} doped polymeric film," Opt. Exp. **17**, 10767–10772 (2009).
6. S. Karaveli and R. Zia, "Spectral tuning by selective enhancement of electric and magnetic dipole emission," Phys. Rev. Lett. **106**, 193004 (2011).
7. X. Ni, G. V. Naik, A. V. Kildishev, Y. Barnakov, A. Boltasseva, and V. M. Shalaev, "Effect of metallic and hyperbolic metamaterial surfaces on electric and magnetic dipole emission transitions," Appl. Phys. B: Lasers Opt. **103**, 553–558 (2011).
8. T. H. Taminiau, S. Karaveli, N. F. van Hulst, and R. Zia, "Quantifying the magnetic nature of light emission," Nat. Commun. **3**, 979 (2012).
9. S. Karaveli, A. J. Weinstein, and R. Zia, "Direct modulation of lanthanide emission at sub-lifetime scales," Nano letters **13**, 2264–2269 (2013).
10. S. Karaveli, S. Wang, G. Xiao, and R. Zia, "Time-resolved energy-momentum spectroscopy of electric and magnetic dipole transitions in Cr^{3+}:MgO," ACS Nano **7**, 7165–7172 (2013).
11. N. Noginova, R. Hussain, M. A. Noginov, J. Vella, and A. Urbas, "Modification of electric and magnetic dipole emission in anisotropic plasmonic systems," Opt. Exp. **21**, 23087–23096 (2013).

12. R. Hussain, D. Keene, N. Noginova, and M. Durach, "Spontaneous emission of electric and magnetic dipoles in the vicinity of thin and thick metal," Opt. Exp. **22**, 7744–7755 (2014).
13. L. Aigouy, A. Cazé, P. Gredin, M. Mortier, and R. Carminati, "Mapping and quantifying electric and magnetic dipole luminescence at the nanoscale," Phys. Rev. Lett. **113**, 076101 (2014).
14. D. Li, M. Jiang, S. Cueff, C. M. Dodson, S. Karaveli, and R. Zia, "Quantifying and controlling the magnetic dipole contribution to 1.5 μm light emission in erbium-doped yttrium oxide," Phys. Rev. B **89**, 161409 (2014).
15. C. Enkrich, M. Wegener, S. Linden, S. Burger, L. Zschiedrich, F. Schmidt, J. F. Zhou, T. Koschny, and C. M. Soukoulis, "Magnetic metamaterials at telecommunication and visible frequencies," Phys. Rev. Lett. **95**, 203901 (2005).
16. L. Novotny, "Effective wavelength scaling for optical antennas," Phys. Rev. Lett. **98**, 266802 (2007).
17. I. Sersic, M. Frimmer, E. Verhagen, and A. F. Koenderink, "Electric and magnetic dipole coupling in near-infrared split-ring metamaterial arrays," Phys. Rev. Lett. **103**, 213902 (2009).
18. T. Grosjean, M. Mivelle, F. I. Baida, G. W. Burr, and U. C. Fischer, "Diabolo nanoantenna for enhancing and confining the magnetic optical field," Nano Lett. **11**, 1009–1013 (2011).
19. S. N. Sheikholeslami, A. García-Etxarri, and J. A. Dionne, "Controlling the interplay of electric and magnetic modes via Fano-like plasmon resonances," Nano Lett. **11**, 3927–3934 (2011).
20. B. Rolly, B. Bebey, S. Bidault, B. Stout, and N. Bonod, "Promoting magnetic dipolar transition in trivalent lanthanide ions with lossless mie resonances," Phys. Rev. B **85**, 245432 (2012).
21. G. Boudarham, R. Abdeddaim, and N. Bonod, "Enhancing the magnetic field intensity with a dielectric gap antenna," Appl. Phys. Lett. **104**, 021117 (2014).
22. R. Paschotta, P. R. Barber, A. C. Tropper, and D. C. Hanna, "Characterization and modeling of thulium: ZBLAN blue upconversion fiber lasers," J. Opt. Soc. Am. B **14**, 1213–1218 (1997).
23. C. P. Wyss, M. Kehrli, T. Huber, P. J. Morris, W. Lüthy, H. P. Weber, A. I. Zagumennyi, Y. D. Zavartsev, P. A. Studenikin, I. A. Shcherbakov, and A. F. Zerrouk, "Excitation of the thulium $^1G_4$ level in various crystal hosts," J. Lumin. **82**, 137 – 144 (1999).
24. A. S. Gouveia-Neto, E. B. da Costa, P. V. dos Santos, L. A. Bueno, and S. J. L. Ribeiro, "Sensitized thulium blue upconversion emission in Nd^{3+}/Tm^{3+}/Yb^{3+} triply doped lead and cadmium germanate glass excited around 800 nm," J. Appl. Phys. **94**, 5678–5681 (2003).
25. F. Auzel, "Upconversion and Anti-Stokes processes with f and d ions in solids," Chem. Rev. **104**, 139–174 (2004).
26. A. S. Gouveia-Neto, L. A. Bueno, R. F. Do Nascimento, E. A. da Silva, E. B. Da Costa, and V. B. Do Nascimento, "White light generation by frequency upconversion in Tm^{3+}/Ho^{3+}/Yb^{3+}-codoped fluorolead germanate glass," Appl. Phys. Lett. **91**, 091114 (2007).
27. S. Fischer, J. C. Goldschmidt, P. Löper, G. H. Bauer, R. Brüggemann, K. Krämer, D. Biner, M. Hermle, and S. W. Glunz, "Enhancement of silicon solar cell efficiency by upconversion: Optical and electrical characterization," J. Appl. Phys. **108**, 044912 (2010).
28. H. Zhang, Y. Li, I. A. Ivanov, Y. Qu, Y. Huang, and X. Duan, "Plasmonic modulation of the upconversion fluorescence in $NaYF_4$:Yb/Tm hexaplate nanocrystals using gold nanoparticles or nanoshells," Angew. Chem. Int. Edit. **49**, 2865–2868 (2010).
29. F. Wang, R. Deng, J. Wang, Q. Wang, Y. Han, H. Zhu, X. Chen, and X. Liu, "Tuning upconversion through energy migration in core–shell nanoparticles," Nature Mater. **10**, 968–973 (2011).
30. E. M. Chan, D. J. Gargas, P. J. Schuck, and D. J. Milliron, "Concentrating and recycling energy in lanthanide codopants for efficient and spectrally pure emission: The case of $NaYF_4$:Er^{3+}/Tm^{3+} upconverting nanocrystals," J. Phys. Chem. B **116**, 10561–10570 (2012).
31. C. Lantigua, S. He, M. A. Bouzan, W. Hayenga, N. J. J. Johnson, A. Almutairi, and M. Khajavikhan, "Engineering upconversion emission spectra using plasmonic nanocavities," Opt. Lett. **39**, 3710–3713 (2014).
32. C. M. Dodson, J. A. Kurvits, D. Li, and R. Zia, "Wide-angle energy-momentum spectroscopy," Opt. Lett. **39**, 3927–3930 (2014).
33. Z. Hong, W. L. Li, D. Zhao, C. Liang, X. Liu, J. Peng, and D. Zhao, "White light emission from OEL devices based on organic dysprosium-complex," Synthetic Met. **111–112**, 43 – 45 (2000).
34. G. Kaur and S. B. Rai, "Cool white light emission in dysprosium and salicylic acid doped poly vinyl alcohol film under UV excitation," J. Fluoresc. **22**, 475–483 (2012).
35. D. K. Sardar, W. M. Bradley, R. M. Yow, J. B. Gruber, and B. Zandi, "Optical transitions and absorption intensities of Dy^{3+} ($4f^9$) in YSGG laser host," J. Lumin. **106**, 195–203 (2004).
36. P. Haro-González, L. Martín, I. Martín, G. Grazyna Dominiak-Dzik, and W. Ryba-Romanowski, "Pump and probe measurements of optical amplification at 584nm in dysprosium doped lithium niobate crystal," Optical Materials **33**, 196–199 (2010).
37. S. R. Bowman, S. O'Connor, and N. J. Condon, "Diode pumped yellow dysprosium lasers," Opt. Exp. **20**, 12906–12911 (2012).
38. F. Vetrone, J.-C. Boyer, J. A. Capobianco, A. Speghini, and M. Bettinelli, "A spectroscopic investigation of trivalent lanthanide doped Y_2O_3 nanocrystals," Nanotechnology **15**, 75 (2004).
39. G. Dominiak-Dzik, P. Solarz, W. Ryba-Romanowski, E. Beregi, and L. Kovács, "Dysprosium-doped $YAl_3(BO_3)_4$

(YAB) crystals: an investigation of radiative and non-radiative processes," J. Alloys Compd. **359**, 51–58 (2003).

40. G. Dominiak-Dzik, W. Ryba-Romanowski, M. N. Palatnikov, N. V. Sidorov, and V. T. Kalinnikov, "Dysprosium-doped $LiNbO_3$ crystal. optical properties and effect of temperature on fluorescence dynamics," J. Mol. Struct. **704**, 139–144 (2004).
41. D. Parisi, A. Toncelli, M. Tonelli, E. Cavalli, E. Bovero, and A. Belleti, "Optical spectroscopy of $BaY_2F_8:Dy^{3+}$," J. Phys. Condens. Matter **17**, 2783–2790 (2005).
42. R. Faoro, F. Moglia, M. Tonelli, N. Magnani, and E. Cavalli, "Energy levels and emission parameters of the Dy3+ ion doped into the YPO_4 host lattice," J. Phys. Condens. Matter **21**, 275501 (2009).
43. M. J. Weber, "Radiative and multiphonon relaxation of rare-earth ions in Y_2O_3," Phys. Rev. **171**, 283–291 (1968).
44. C. Guery, J. L. Adam, and J. Lucas, "Optical properties of Tm^{3+} ions in indium-based fluoride glasses," J. Lumin. **42**, 181–189 (1988).
45. I. Sokólska, W. Ryba-Romanowski, S. Gołąb, M. Baba, M. Świrkowicz, and T. Łukasiewicz, "Spectroscopy of $LiTaO_3:Tm^{3+}$ crystals," J. Phys. Chem. Solids **61**, 1573–1581 (2000).
46. W. A. Pisarski, J. Pisarska, G. Dominiak-Dzik, and W. Ryba-Romanowski, "Visible and infrared spectroscopy of Pr^{3+} and Tm^{3+} ions in lead borate glasses," J. Phys. Condens. Matter **16**, 6171 (2004).
47. Y. Guyot, R. Moncorgé, L. D. Merkle, A. Pinto, B. McIntosh, and H. Verdun, "Luminescence properties of Y_2O_3 single crystals doped with Pr^{3+} or Tm^{3+} and codoped with Yb^{3+}, Tb^{3+} or Ho^{3+} ions," Opt. Mater. **5**, 127 – 136 (1996).

1. Introduction

Optical-frequency magnetic dipole (MD) transitions have garnered interest recently as a way for naturally occurring emitters to interact with the magnetic component of light. As a result of recent theoretical [1–4] and experimental [5–14] studies, the need for MD transitions with emission wavelengths in the NIR has increased. Longer wavelengths ease nanofabrication complexities by allowing for larger structure dimensions as well as lower Ohmic losses. These structures could then be leveraged to enhance the magnetic dipole contribution to overall light emission [15–21]. Thus, to help realize technologically relevant devices, we must identify and characterize strong MD emission lines in the NIR that could serve as resonant sources.

Here, we use energy- and momentum-resolved spectroscopy to directly quantify the electric and magnetic dipole contributions to light emission from transitions in Dy^{3+} and Tm^{3+} doped Y_2O_3. Many of these emission lines have been explored for use in upconversion processes where they can be used as the energy transfer donor or acceptor ion [22–31]. Of the emission lines in these ions, we find that the overlapping $^4F_{9/2} \rightarrow {}^6F_{11/2}$ and $^4F_{9/2} \rightarrow {}^6H_{9/2}$ transitions in Dy^{3+} and the $^1G_4 \rightarrow {}^3H_5$ transition in Tm^{3+} exhibit significant MD contributions and offer the best pathways to optical frequency MD enhancement. This work shows how the NIR emission lines of these lanthanide ions could serve as the basis for investigation of magnetic light-matter interactions with optical metamaterials and nanoantennas.

We can first examine the likelihood of MD mediated emission from an initial state $|\psi_i\rangle$. To this end, using the previously measured lifetime of the excited levels and calculated spontaneous emission rates for the MD allowed transitions originating from these levels, we can estimate the likely MD branching ratios. We calculate the branching ratio for all MD mediated transitions using

$$\beta_{MD} = \tau \sum_f A_{MD,f}. \tag{1}$$

Here f runs over all possible decay levels, $|\psi_f\rangle$. $A_{MD,f}$ is the MD spontaneous emission rate to a specific level, and τ is the excited level lifetime. This offers a glimpse at the overall MD branching ratio, from $|\psi_i\rangle$, but it fails to shed light on the respective MD contribution, a_{MD}, for each individual transition. Relationships between these values can be found in Table 1.

By using energy-momentum spectroscopy [8], we can experimentally quantify the spectrally resolved electric dipole (ED) and MD emission rates, thereby examining the fractional contribution that a particular dipole transition plays in radiative decay between two levels. We use this technique to measure the energy-momentum spectra for each of the NIR emission lines in Dy^{3+}
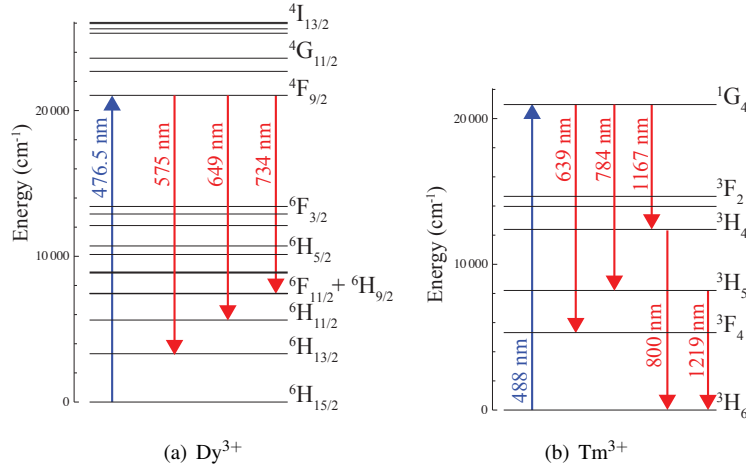
(a) Dy^{3+} (b) Tm^{3+}

Fig. 1: Free ion energy level diagrams of Dy^{3+} and Tm^{3+}. Note that introduction of ions into Y_2O_3 host slightly shifts the energy levels and transition wavelengths.

and Tm^{3+}, see Fig. 1. These fits yield the ED and MD emission rates by fitting the measured data to analytical theory of isotropic ED and MD momentum cross-sections at each wavelength. Integrating the spectrally resolved emission rates over all wavelengths in the measurement domain allows us to determine the total percentage of ED and MD emission for the transitions of interest. In the case of spectrally distinct transitions, we obtain the total ED and MD emission. We can convert these extracted emission rates to absolute intrinsic emission rates, a_{ED} and a_{MD}, by using the methods presented in [14] and the spontaneous emission rates shown in Tables 2 and 3. In the case of spectrally overlapping transitions, we are restricted to relative emission rates for the particular spectral region.

Table 1: Terminology for branching ratios and emission rates. The subscripts r and nr denote radiative and non-radiative decay, while i and f label the initial and final levels of a particular transition. Note that while we have listed a_{MD}, the same relationships hold for a_{ED} with the substitution $\Gamma_{MD} \to \Gamma_{ED}$ in the numerator.

$\Gamma_{total,i \to f}$	$=$	$\Gamma_{r,i \to f} + \Gamma_{nr,i \to f}$
$\beta_{i \to f}$	:	The contribution of a particular transition to the total decay of an excited state.
	$=$	$\dfrac{\Gamma_{r,i \to f}}{\sum_f \Gamma_{r,i \to f} + \Gamma_{nr}}$,
	where	$\sum_f \Gamma_{r,i \to f} + \Gamma_{nr} = \dfrac{1}{\tau}$
a_{MD}	:	The fractional contribution of MD transitions to a specific radiative transition.
	$=$	$\dfrac{\Gamma_{MD,i \to f}}{\Gamma_{ED,i \to f} + \Gamma_{MD,i \to f}}$

2. Experimental details

2.1. Sample fabrication

We fabricated luminescent thin films of Dy^{3+} doped Y_2O_3 and Tm^{3+} doped Y_2O_3 by physical vapor deposition and subsequent annealing. First, undoped yttria buffer layers were deposited onto quartz coverslips by electron beam evaporation (20 nm in thickness for the Dy doped samples and 60 nm for the Tm doped samples). Then, lanthanide doped (5% by weight) yttria layers (20 nm for Dy and 50 nm Tm) were deposited followed by a 10 nm undoped yttria capping layer. The buffer and capping layers were included to improve the crystallinity of the thin films and enhance the resulting emission [14]. Following the depositions, the samples were annealed at 1000°C for 1 hour in a dry O_2 tube furnace in order to activate the emitters. The thickness was determined by measuring the film depositions in situ with a quartz crystal microbalance and then subsequently confirmed via ellipsometry.

2.2. Experimental setup

Dy^{3+} and Tm^{3+} ions were excited using the 476.5 nm and 488 nm lines of an argon ion laser, respectively. The experimental setup is the same as that used in [32] in which a 1.3 NA oil immersion objective (Nikon Plan Fluor 100x) was used both to excite the samples as well as collect the emission. A Bertrand lens imaged the back focal plane of the objective through a Wollaston prism, allowing for simultaneous imaging of two orthogonal polarizations. These images were projected onto the entrance slit of a Schmidt-Czerny-Turner imaging spectrograph (Princeton Instruments IsoPlane SCT-320), dispersed by a grating and then imaged using either a silicon based imaging camera (Princeton Instruments Pixis 1024B) for visible wavelengths (all Dy^{3+} emission lines as well as the 639 and 800 nm emission lines in Tm^{3+}) or an InGaAs based imaging detector (Princeton Instruments NIRvana) for the 1200 nm emission in Tm^{3+}.

3. Results and discussion

3.1. Dy^{3+}:Y_2O_3

Dysprosium emission primarily has been explored in regards to the $^4F_{9/2} \rightarrow {}^6H_{13/2}$ line around 575 nm. This yellow emission is desirable for applications in solid-state lighting [33, 34], lasers [35–37], and dysprosium-based upconversion processes [25, 29]. However, there are many other emission lines in Dy^{3+} that have received far less attention due to their weaker luminescence. Our previous calculations have suggested that these emission lines could be promising for applications as MD sources for optical antennas and other resonant nanostructures [1].

There are three MD emission lines of interest, the $^4F_{9/2} \rightarrow {}^6H_{11/2}$ transition as well as the spectrally overlapping $^4F_{9/2} \rightarrow {}^6F_{11/2}$ and $^4F_{9/2} \rightarrow {}^6H_{9/2}$ transitions. These levels and transitions are shown in Fig. 1(a), which also includes for completeness, the $^4F_{9/2} \rightarrow {}^6H_{13/2}$ ED transition and the $^6H_{15/2} \rightarrow {}^4F_{9/2}$ absorption transition used for excitation. These transitions all originate from the same $^4F_{9/2}$ excited level, and by using Eq. (1) with the previously measured excited level lifetime of 706 μs [38], we find that MD transitions should account for at least 6.8% of all radiative decay from the $^4F_{9/2}$ level.

As shown in Table 2, the $^4F_{9/2} \rightarrow {}^6H_{11/2}$ transition has a branching ratio of 1.08%. If we instead examine the MD contribution to this particular transition, shown in Fig. 2, we see that this transition is predominantly ED. Figure 2c shows two representative cross-sections of the experimental measurements (solid) and theoretical fits (dashed) at 658.5 nm and 668.8 nm, respectively. At each wavelength, fitting the cross-sections yields the respective ED and MD contribution. Performing this fit at each wavelength yields the emission rates shown in Fig. 2e.

Table 2: Summary of MD emission in Dy^{3+}:Y_2O_3. Here, i and f define the initial and final levels of the transition. τ denotes the excited level lifetime that is used in calculations of β. $A = A'n_r^3$, where A' is the vacuum emission rate presented in [1] and n_r=1.72 is the refractive index for the thin films of Y_2O_3. $\beta_{i \to f,MD}$ is the fractional contribution of MD emission of all radiative decay from the i to f level and a_{MD} is the relative percentage of MD emission for the specific transition(s). The spectral regions associated with each transition, or overlapping transitions, are defined by the plot ranges in Fig. 2-3.

i	f	τ (μs)	λ (nm)	A_{MD} (s^{-1})	$\beta_{i \to f,MD}$	a_{MD}
$^4F_{9/2} \to$	$^6H_{11/2}$	706 [38]	649	15.37	1.08%	8.5%
	$^6F_{11/2}$		734	59.53	4.2%	35.2%
	$^6H_{9/2}$		736	3.54	0.2%	
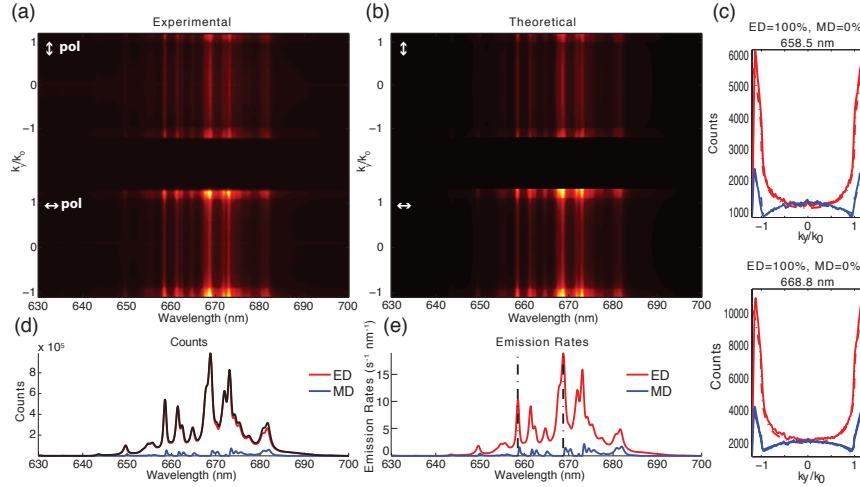
Fig. 2: Energy-momentum spectra of $^4F_{9/2} \to {}^6H_{11/2}$ transition in Dy^{3+}:Y_2O_3. (a) Polarized experimental data and (b) corresponding fits. (c) Representative polarized cross-sections of experimental data (solid) and theoretical fits (dashed) at 658.5 nm and 668.8 nm. Both wavelengths show emission that is 100% ED with 0% MD contribution. Vertical polarization is shown in blue and horizontal polarization is shown in red. (d) Total (black) counts for ED (red) and MD (blue) emission. (e) Intrinsic emission rates for ED (red) and MD (blue) emission. The wavelengths of each cross-section are marked with dashed black lines. The white arrows in (a,b) denote polarization.

By integrating these rates over the measurement domain, we find that this particular transition has a_{ED}=91.5% and a_{MD}=8.5%. The overall branching ratio can then be estimated, $\beta_{i \to f} = \beta_{i \to f,MD}/a_{MD}$=12.7%, which is significantly higher than previous calculations in various crystal hosts with branching ratios ranging from 2.2% in $Y_3Sc_2Ga_3O_{12}$ (YSGG) to 7.4% in $YAl_3(BO_3)_4$ (YAB) [35, 39–42].

In addition to this visible emission line, we also examine additional lines originating from the $^4F_{9/2}$ level that emit at longer wavelengths. These include the $^4F_{9/2} \to {}^6F_{11/2}$ and $^4F_{9/2} \to$ $^6H_{9/2}$ transitions with overlapping emission around 750 nm. Table 2 suggests that this emission
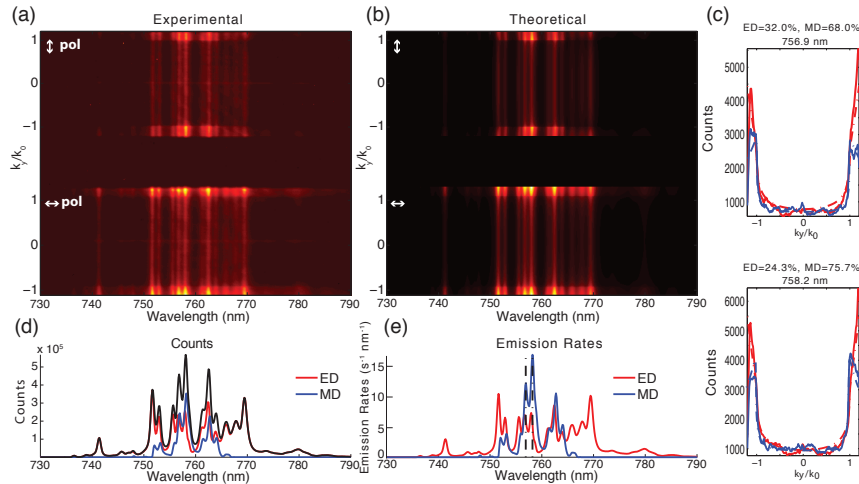
Fig. 3: Energy-momentum spectra of $^4F_{9/2} \rightarrow {}^6F_{11/2}$ and $^4F_{9/2} \rightarrow {}^6H_{9/2}$ transitions in Dy^{3+}:Y_2O_3. (a) Polarized experimental data and (b) corresponding fits. (c) Representative polarized cross-sections of experimental data (solid) and theoretical fits (dashed) at 756.9 nm, 32.0% ED and 68.0% MD, and 758.2 nm, 24.3% ED and 75.7% MD. Vertical polarization is shown in blue and horizontal polarization is shown in red. (d) Total (black) counts for ED (red) and MD (blue) emission. (e) Intrinsic emission rates for ED (red) and MD (blue) emission. The wavelengths of each cross-section are marked with dashed black lines. The white arrows in (a,b) denote polarization.

should have a strong MD component, A_{MD}=59.53 s^{-1}. The MD emission from both transitions should account for at least 4.4% of the overall radiative decay from the $^4F_{9/2}$ level. Though it is an unlikely decay pathway from the $^4F_{9/2}$ excited level, the emission from these overlapping transitions exhibit strong MD contributions. Integrating the emission rates in Fig. 3, from 730 to 790 nm, yields a_{ED}=64.8% and a_{MD}=35.2%. This large fractional contribution suggests that this transition, while relatively weak, has a significant MD component. The branching ratio for the combined transitions is 12.5% of the total radiative decay from the $^4F_{9/2}$ level, roughly 4× larger than in other materials [35, 39–42] suggesting the importance of crystal hosts.

3.2. Tm^{3+}:Y_2O_3

From the level structure of Tm^{3+} free ions, shown in Fig. 1(b), we see that there are several low lying transitions of interest. Using the 488 nm line from an argon ion laser, we excite from the $^3H_6$ ground level to the $^1G_4$ excited level. From this level, there are four nonzero MD transitions [1] of which we examine three: the $^1G_4 \rightarrow {}^3F_4$, $^1G_4 \rightarrow {}^3H_4$, and $^1G_4 \rightarrow {}^3H_5$ transitions. In particular, we highlight the $^1G_4 \rightarrow {}^3H_4$ decay path, because $^3H_4$ is the excited level for the ED mediated $^3H_4 \rightarrow {}^3H_6$ transition that spectrally overlaps with the $^1G_4 \rightarrow {}^3H_5$ transition. We exclude the $^1G_4 \rightarrow {}^3F_3$ transition, because it exhibits emission near 1400 nm. Finally, we examine the MD contribution of the $^3H_5 \rightarrow {}^3H_6$ transition which overlaps with the $^1G_4 \rightarrow {}^3H_4$ emission near 1200 nm. A summary of these MD transitions, corresponding emission rates, and branching ratios can be found in Table 3. Due to this energy level structure, Tm^{3+} has been used as both the donor and acceptor in multi-ion upconversion processes [22–26, 28, 30, 31].

We first examine the emission from the $^1G_4 \rightarrow {}^3F_4$ transition by means of energy-momentum

Table 3: Summary of MD emission in Tm^{3+}:Y_2O_3. Here, i and f define the initial and final levels of the transition. τ denotes the excited level lifetime that is used in calculations of β. $A = A'n_r^3$, where A' is the vacuum emission rate presented in [1] and n_r=1.72 is the refractive index for the thin films of Y_2O_3. $\beta_{i \to f,MD}$ is the fractional contribution of MD emission of all radiative decay from the i to f level and a_{MD} is the relative percentage of MD emission for the specific transition(s). The spectral regions associated with each transition, or overlapping transitions, are defined by the plot ranges in Fig. 4-6.

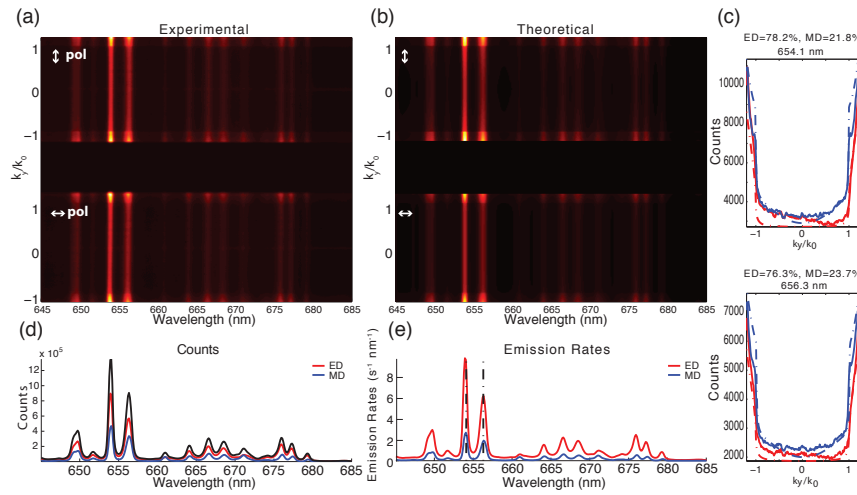| i	f	τ (μs)	λ (nm)	A_{MD} (s^{-1})	$\beta_{i \to f,MD}$	a_{MD}
$^1G_4 \to$	$^3F_4$	135 [38]	639	9.72	0.13%	18.2%
	$^3H_5$		800	115.00	1.6%	$\geq$18.0%
	$^3H_4$		1167	28.50	0.38%	17.8%
$^3H_5 \to$	$^3H_6$	300 [43]	1200	73.78	2.21%	

Fig. 4: Energy-momentum spectra of $^1G_4 \to {}^3F_4$ transition in Tm^{3+}:Y_2O_3. (a) Polarized experimental data and (b) corresponding fits. (c) Representative polarized cross-sections of experimental data (solid) and theoretical fits (dashed) at 654.1 nm, 78.2% ED and 21.8% MD, and 656.3 nm, 76.3% ED and 23.7% MD. Vertical polarization is shown in blue and horizontal polarization is shown in red. (d) Total (black) counts for ED (red) and MD (blue) emission. (e) Intrinsic emission rates for ED (red) and MD (blue) emission. The wavelengths of each cross-section are marked with dashed black lines. The white arrows in (a,b) denote polarization.

spectroscopy. Figure 4 shows the energy-momentum spectra and theoretical fits as well as two representative cross-sections, at 654.1 and 656.3 nm, that correspond to peaks in the emission spectrum. By integrating the extracted intrinsic emission rates in Fig. 4(e), we find that the emission from this specific transition is 18.2% MD (a_{MD} = 18.2%, a_{ED} = 81.8%). We can infer then that the branching ratio for the $^1G_4 \to {}^3F_4$ transition is $\beta_{i \to f}$=20.6%, which is ∼2x greater than previous estimations for this transition [44–46].

Examining the emission at 800 nm from the $^1G_4 \to {}^3H_5$ transition, see Fig. 5, we find a_{ED}=82.0% and a_{MD}=18.0%, which may seem low for an MD spontaneous emission rate of A=115 s^{-1}. This lower than expected a_{MD} is likely due to the overlapping $^3H_4 \to {}^3H_6$ tran-
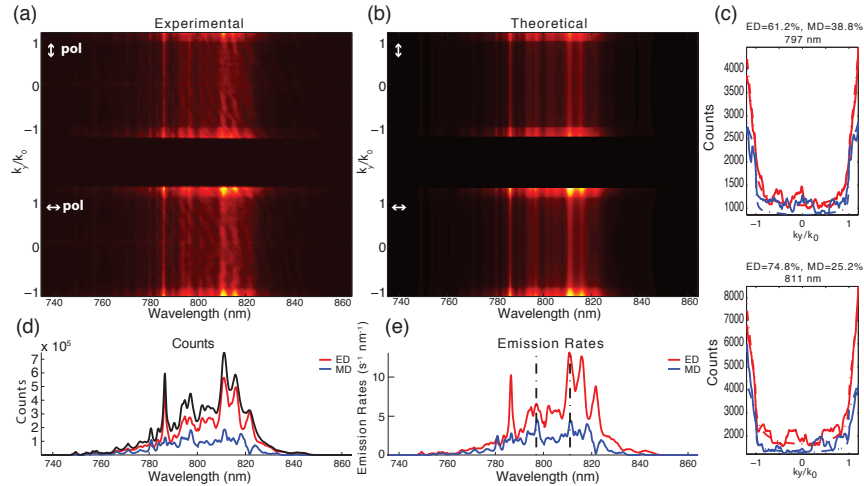
Fig. 5: Energy-momentum spectra of $^1G_4 \to {}^3H_5$ and $^3H_4 \to {}^3H_6$ transitions in Tm^{3+}:Y_2O_3. (a) Experimental data and (b) corresponding fits. (c) Vertically (blue) and horizontally (red) polarized cross-sections of experimental data (solid) and theoretical fits (dashed) at 797 nm, 61.2% ED and 38.8% MD, and 811 nm, 74.8% ED and 25.2% MD. (d) Total (black) counts for ED (red) and MD (blue) emission. (e) Intrinsic emission rates for ED (red) and MD (blue) emission. The wavelengths of each cross-section are marked with dashed black lines. The white arrows in (a,b) denote polarization.

sition [47], which is MD forbidden and is calculated to be the dominant decay path from the $^3H_4$ level [44, 45]. Given that this transition is only allowed by ED emission, we can estimate a lower bound for the branching ratio. The $^1G_4 \to {}^3H_5$ transition accounts for $\geq 0.21\%$ of the total radiative decay from the $^1G_4$ excited level. By enhancing the MD emission, while suppressing ED emission, one could further study the $^1G_4 \to {}^3H_5$ transition and determine better bounds on the MD emission.

Tm^{3+} ions also exhibit emission at longer wavelengths, such as the $^1G_4 \to {}^3H_4$ and $^3H_5 \to {}^3H_6$ transitions at $\sim$1150 and $\sim$1200 nm, respectively. Emission from the $^3H_5 \to {}^3H_6$ transition has been exploited for upconversion applications using Yb^{3+}-Tm^{3+} codoped core-shell nanoparticles [29] and accounts for 99% of the radiative decay from the $^3H_5$ level [46]. Integrating the emission rates in Fig. 6e, we find that the total emission from the two transitions is a_{ED}=82.2% and a_{MD}=17.8%. Though the $^3H_5 \to {}^3H_6$ transition is calculated to have a large spontaneous emission rate, the MD branching ratio for the $^3H_5$ transition is a fairly low 2.2% suggesting that other decay pathways are more likely. Representative experimental cross-sections and corresponding theoretical fits for emission at 1208.6 nm and 1271.5 nm, see Fig. 6, show good agreement despite the noise from the experimental measurements.
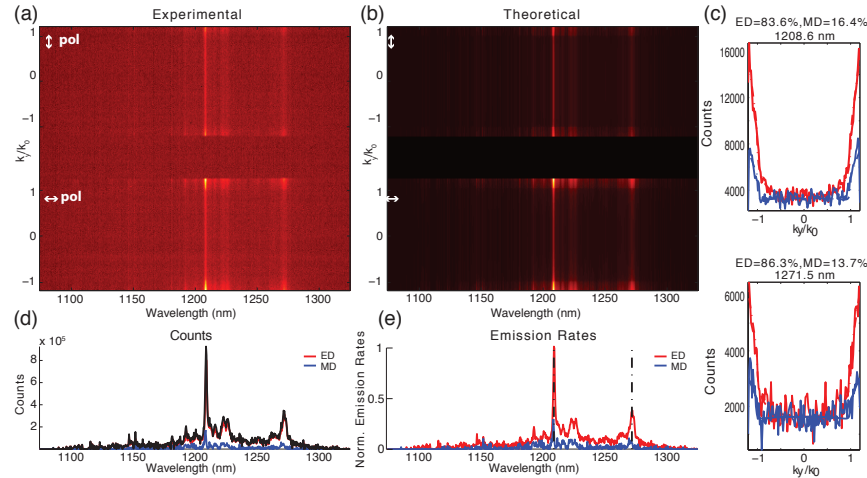
Fig. 6: Energy-momentum spectra of $^1G_4 \rightarrow {}^3H_4$ and $^3H_5 \rightarrow {}^3H_6$ transitions in Tm^{3+}:Y_2O_3. (a) Experimental data and (b) corresponding fits. (c) Vertically (blue) and horizontally (red) polarized cross-sections of experimental data (solid) and theoretical fits (dashed) at 1208.6 nm, 83.6% ED and 16.4% MD, and 1271.5 nm, 86.3% ED and 13.7% MD. (d) Total (black) counts for ED (red) and MD (blue) emission. (e) Normalized emission rates for ED (red) and MD (blue) emission. The wavelengths of each cross-section are marked with dashed black lines. The white arrows in (a,b) denote polarization.

4. Conclusion

Magnetic dipole emission lines in the NIR region could have broad applications in resonant nanostructures due primarily to the benefits of operating at longer wavelengths (easier fabrication of structures as well as lower Ohmic losses). We characterized the emission rates for multiple transitions in Dy^{3+} and Tm^{3+} doped Y_2O_3. These lines could play important roles in various applications, including imaging and energy based upconversion processes. While these emission lines were previously calculated to have large spontaneous emission rates, we find that the MD contribution to the overall emission is low. Further, we report that the overlapping $^4F_{9/2} \rightarrow {}^6F_{11/2}$ and $^4F_{9/2} \rightarrow {}^6H_{9/2}$ transitions in Dy^{3+}, centered at 750 nm, as well as the $^1G_4 \rightarrow {}^3H_5$ and $^3H_4 \rightarrow {}^3H_6$ transitions in Tm^{3+} show the greatest MD contributions, and thus provide the best pathways for future study. Other transitions in Dy^{3+} and Tm^{3+} were also characterized, but we find that their MD contributions in Y_2O_3 are relatively low. Though several of these emission lines have low MD contributions, they operate in the NIR where resonant structures are easier to fabricate and characterize. By integrating Dy^{3+} and Tm^{3+} with resonant nanostructures, one could enhance and engineer these MD emission lines to better leverage upconversion processes for use in energy harvesting and biological imaging.